Int. J. Heat Mass Transfer. Vol. 37, No. 1, pp. 13–26, 1994
Printed in Great Britain

0017–9310/94 $6.00 + 0.00

Effect of the orientation of a finned surface on the melting of frozen porous media

K. SASAGUCHI
Department of Mechanical Engineering, Kumamoto University, Kumamoto 860, Japan

and

H. TAKEO
Honda Motors Co. Ltd., Houga-machi, Houga-gun, Tochigi 321-33, Japan

(*Received* 28 *April* 1993 *and in final form* 19 *July* 1993)

Abstract—Numerical calculations were performed for the melting process in porous media around a hot surface with conducting fins (fins with a large thermal-conductivity). The effect of the orientation of the hot surface on the effectiveness of the attached fins was examined. Three orientations, that is, the melting from below, from the side and from above, were selected as typical ones. Timewise variations of a temperature distribution, a velocity distribution, an interface shape, a mean Nusselt number and a melting fraction were compared. As a result, the temperature and flow fields became very complicated due to the attached conducting fins, especially in the cases of melting from below and from the side. The mean Nusselt number, $(\overline{Nu})_w$, over the hot surface for the melting from below was kept large for a long time, and varied irregularly with time. The value of $(\overline{Nu})_w$ for the melting from above decreased monotonously with time. The melting rate was the largest for the melting from below, and the smallest for the melting from above, while the effect of the fins appeared relatively larger for the melting from above.

1. INTRODUCTION

SOLID/LIQUID phase change heat transfer in saturated porous media occurs in many systems and in nature including latent heat thermal energy storage, manufacturing of alloys, freezing and thawing of soil, and so forth. Therefore, studies on this subject have been actively conducted [1–7].

Chellaiah and Viskanta [1] studied freezing of saturated and superheated water in porous media packed in a rectangular cavity. They performed one-dimensional calculations considering conduction alone. The calculated results agreed well with experimental ones when the water superheat (the difference between an initial temperature and the freezing point temperature) was small, but the agreement was not good for a large superheat and for a large size of porous particles, due to natural convection. Considering natural convection, Beckermann and Viskanta [2], and Sasaki *et al.* [3] proposed a numerical model to simulate solid/liquid phase change of fluid in porous media. They performed two-dimensional calculations for a rectangular cavity, and their results agreed well with experimental ones even when natural convection was important. Okada and Fukumoto [4] numerically studied the melting of ice around a cylinder immersed in porous media. They also took natural convection into account, and the numerically obtained interface shapes were in good agreement with experimental ones. They also examined effects of Stefan number and Rayleigh number on the melting rate. The effect of the density inversion of water was examined numerically and experimentally for freezing from above by Sugawara *et al.* [5], and for melting from below by Xhang and Nguyen [6]. They used rectangular cavities, and indicated that the density inversion largely affected the fluid flow in the melt and the heat transfer.

The heat transfer rate in solid/liquid phase change in porous media is usually small due to small thermal conductivities of phase change material and porous particles. Some means must be devised to enhance the heat transfer, especially for thermal-energy-storage applications. Therefore, one of the authors, Sasaguchi, and Kusano and Nishimizu [7] experimentally and numerically studied the solidification process around finned surfaces in porous media, and showed the usefulness of the fins.

In the present study, a numerical model was proposed to simulate the solid/liquid phase change heat transfer in porous media around a finned surface, based on a model proposed by Bennon and Incropera [8]. Calculations were performed for three orientations of the finned surface, that is, melting from below, from the side and from above, to examine the effect of natural convection on the heat transfer. Calculations were also performed for the case with nonconducting fins (fins with a zero thermal-conductivity) to make the effect of the attached conducting-fins clear.

NOMENCLATURE

a thermal diffusivity
A_s aspect ratio, L_x/L_y
c specific heat
d diameter of porous particles
g gravitational acceleration
h_f latent heat of fusion
h heat transfer coefficient
(I, J) grid point
K permeability
L_x width of test element (see Fig. 1)
L_y height of the test element (see Fig. 1)
p pressure
R melting fraction
t time
T temperature
u, v x-, y-direction mass-averaged velocity components
V_{sc} scale of magnitude of dimensionless velocity vector
V_{MAX} maximum of magnitude of the dimensionless velocity vector
x, y coordinate axes (see Fig. 1)
$(\vec{\ })$ vector.

Greek symbols
β thermal expansion coefficient
γ volume fraction
$\Delta\theta$ increment of isotherms
δ thickness of fins
ε porosity
λ thermal conductivity
ν kinematic viscosity
ρ density
ϕ angle between the center line of the test element and the horizon (see Fig. 1), or variables, U, V, θ or γ_1 in equations (16) and (17).

Subscripts
F fin
F1 fin-1 (see Fig. 1)
F2 fin-2 (see Fig. 1)
i initial
l liquid phase
p porous particles
PH fusion point
s solid phase
w hot wall
x x-direction
y y-direction.

2. A NUMERICAL MODEL AND GOVERNING EQUATIONS

Figure 1 shows the physical model on which the numerical analysis was performed. It consists of a hot wall, an opposite insulated wall, and conducting fins with thickness of δ connecting the two walls. A porous medium is packed in the enclosed region, and for simplicity the number of fins is assumed infinite so that we only need to consider one element shown in Fig. 1(b). Solid (ice in this study) in the pores is initially set at the fusion temperature. At time $t = 0$ s, the temperature of the hot wall is suddenly changed and maintained at a prescribed value, T_w, which is larger than the fusion temperature, and the melting is initiated. To examine the effect of the orientation of the hot wall on the melting, the angle ϕ in Fig. 1 was set at 0° (melting from below), 90° (from the side) or 180° (from above). Timewise variations of an interface shape, a melting fraction and a mean Nusselt number over the hot wall were compared. In addition, calculations for a hot wall with nonconducting fins were also performed for comparison.

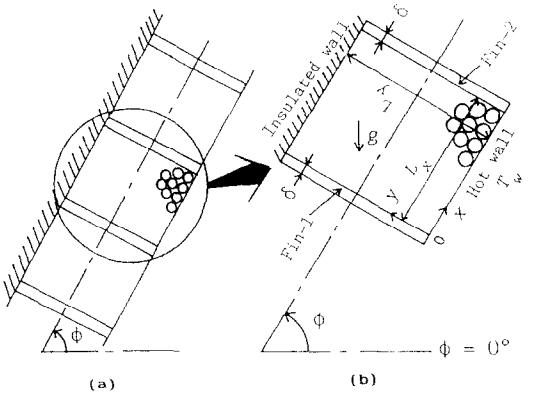

FIG. 1. Physical model: (a) enclosure with a finned surface and (b) element for calculation.

Assuming a two-dimensional laminar flow, constant density except buoyancy terms in momentum equations, an isotropic porous medium, thin fins (no temperature gradient in the direction of the fin width (the x-direction in Fig. 1)) and local thermal equilibrium (i.e. the temperature of a porous particle is locally equal to that of surrounding fluid), as well as modifying equations proposed by Bennon and Incropera [8] to apply them to the present problem, the governing equations in dimensional forms can be derived as follows:

Continuity

$$\frac{\partial u}{\partial x} + \frac{\partial v}{\partial y} = 0. \tag{1}$$

Momentum
(i) X-direction

$$\rho\frac{\partial u}{\partial t}+\rho\nabla\cdot(\vec{v}u)=-\frac{\partial p}{\partial x}+\rho\nu_l\nabla^2u-\rho\frac{\nu_l}{K_x}u+b_x, \quad (2)$$

where

$$b_x=\rho_l g\sin\phi\gamma_l(T-T_{PH})\{\beta_1+\beta_2(T-T_{PH})+\beta_3(T-T_{PH})^2+\beta_4(T-T_{PH})^3\},$$

and, according to ref. [9],

$$\beta_1=-0.678964520\times10^{-4}(1/K),$$
$$\beta_2=0.907294338\times10^{-5}(1/K^2),$$
$$\beta_3=-0.964568125\times10^{-7}(1/K^3),$$
$$\beta_4=0.873702983\times10^{-9}(1/K^4).$$

(ii) Y-direction

$$\rho\frac{\partial v}{\partial t}+\rho\nabla\cdot(\vec{v}v)=-\frac{\partial p}{\partial y}+\rho\nu_l\nabla^2v-\rho\frac{\nu_l}{K_y}v+b_y, \quad (3)$$

where

$$b_y=\rho_l g\cos\phi\gamma_l(T-T_{PH})\{\beta_1+\beta_2(T-T_{PH})+\beta_3(T-T_{PH})^2+\beta_4(T-T_{PH})^3\}.$$

Energy equation for the fluid

$$\rho c\frac{\partial T}{\partial t}+\rho c_l\nabla\cdot(\vec{v}T)=\nabla\cdot(\lambda\nabla T)-\rho_l h_f\frac{\partial\gamma_l}{\partial t}. \quad (4)$$

The second term on the right hand side of equation (4) is a source term related to phase change.

Energy equation for the fins

$$\frac{\partial T_F}{\partial t}=a_F\left\{\frac{\partial^2T_F}{\partial y^2}+\frac{1}{\lambda_F\delta}\left(\lambda\frac{\partial T}{\partial x}\right)_{x=0}-\frac{1}{\lambda_F\delta}\left(\lambda\frac{\partial T}{\partial x}\right)_{x=L_x}\right\}. \quad (5)$$

In the equations (2)–(4), ρ, ρc, and λ are defined as follows:

$$\rho=(1-\varepsilon)\rho_p+\varepsilon\rho_l \text{ (assuming } \rho_l=\rho_s)$$
$$\rho c=(1-\varepsilon)\rho_p c_p+(\varepsilon-\gamma_l)\rho_s c_s+\gamma_l\rho_l c_l$$
$$\lambda=(1-\varepsilon)\lambda_p+(\varepsilon-\gamma_l)\lambda_s+\gamma_l\lambda_l. \quad (6)$$

For buoyancy terms, b_x and b_y, in the momentum equations (2) and (3), the density inversion of water [9] is considered.

Introducing dimensionless quantities,

$$X=\frac{x}{L_x},\quad Y=\frac{y}{L_x},\quad U=\frac{L_x}{a_l}u,\quad V=\frac{L_x}{a_l}v,$$
$$P=\frac{L_x^2p}{\rho_l a_l^2},\quad \tau=\frac{a_l}{L_x^2}t,\quad \theta=\frac{T-T_i}{T_w-T_i},$$

and dimensionless parameters,

$$\theta_{PH}=\frac{T_{PH}-T_i}{T_w-T_i},\quad D_a=\frac{K}{L_x^2},\quad P_r=\frac{\nu_l}{a_l},\quad A_s=\frac{L_x}{L_y},$$
$$R_{aM}=\frac{g\beta_1L_y^3(T_w-T_{PH})}{\nu_l a_l},\quad (S_{te})_M=\frac{c_l(T_w-T_{PH})}{h_f},$$
$$\eta=\frac{\lambda_F}{\lambda_l}\frac{\delta}{L_x},\quad \zeta_F=\frac{a_F}{a_l},\quad \Pi_p=\frac{\rho_p}{\rho_l},\quad \Lambda_p=\frac{\lambda_p}{\lambda_l},$$
$$\Lambda_s=\frac{\lambda_s}{\lambda_l},\quad \Omega_p=\frac{c_p}{c_l},\quad \Omega_s=\frac{c_s}{c_l},$$
$$\alpha_{M1}=\frac{\beta_2}{\beta_1}(T_w-T_{PH}),\quad \alpha_{M2}=\frac{\beta_3}{\beta_1}(T_w-T_{PH})^2,$$
$$\alpha_{M3}=\frac{\beta_4}{\beta_1}(T_w-T_{PH})^3,$$

we may obtain the following nondimensional equations;

Continuity

$$\frac{\partial U}{\partial X}+\frac{\partial V}{\partial Y}=0. \quad (7)$$

Momentum
(i) X-direction

$$\frac{\partial U}{\partial\tau}+\nabla\cdot(\vec{V}U)=-\frac{1}{\Pi}\frac{\partial P}{\partial X}+P_r\nabla^2U-P_r\frac{\kappa}{D_a}U+B_x, \quad (8)$$

where

$$B_x=\gamma_l\frac{A_s^3}{\Pi}P_rR_{aM}\theta_M(1+\alpha_{M1}+\alpha_{M2}\theta_M^2+\alpha_{M3}\theta_M^3)\sin\phi,$$
$$\theta_M=\frac{\theta-\theta_{PH}}{1-\theta_{PH}}.$$

(ii) Y-direction

$$\frac{\partial V}{\partial\tau}+\nabla\cdot(\vec{V}V)=-\frac{1}{\Pi}\frac{\partial P}{\partial Y}+P_r\nabla^2V-P_r\frac{\kappa}{D_a}v+B_y, \quad (9)$$

where

$$B_y=\gamma_l\frac{A_s^3}{\Pi}P_rR_{aM}\theta_M\times(1+\alpha_{M1}\theta_M+\alpha_{M2}\theta_M^2+\alpha_{M3}\theta_M^3)\cos\phi.$$

Energy equation for the fluid

$$\Omega\frac{\partial\theta}{\partial\tau}+\nabla\cdot(\vec{V}\theta)=\frac{1}{\Pi}\nabla\cdot(\Lambda\nabla\theta)+S_h, \quad (10)$$

where

$$S_h=-\frac{1}{\Pi}\frac{1-\theta_{PH}}{(S_{te})_M}\frac{\partial\gamma_l}{\partial\tau},$$
$$\Pi=(1-\varepsilon)\Pi_p+\varepsilon,$$
$$\Omega=[(\Pi-\varepsilon)\Omega_p+(\varepsilon-\gamma_l)\Omega_s+\gamma_l]/\Pi,$$
$$\Lambda=(1-\varepsilon)\Lambda_p+(\varepsilon-\gamma_l)\Lambda_s+\gamma_l.$$

Table 1. Boundary conditions

	U, V	θ	
		With conducting fins	With nonconducting fins
$X=0$	0	θ_{F} (from equation (5))	$\dfrac{\partial\theta}{\partial X}=0$
$X=1$	0	θ_{F} (from equation (5))	$\dfrac{\partial\theta}{\partial X}=0$
$Y=0$	0	1	1
$Y=\dfrac{L_{\mathrm{f}}}{L_{\mathrm{y}}}$	0	$\dfrac{\partial\theta}{\partial Y}=0$	$\dfrac{\partial\theta}{\partial Y}=0$

Energy equation for the fins

$$\frac{\partial\theta_{\mathrm{F}}}{\partial\tau}=\zeta_{\mathrm{F}}\left\{\frac{\partial^2\theta_{\mathrm{F}}}{\partial Y^2}+\frac{1}{\eta}\left(\frac{\partial\theta}{\partial X}\right)_{X=0}-\frac{1}{\eta}\left(\frac{\partial\theta}{\partial X}\right)_{X=1}\right\}. \tag{11}$$

The volumetric liquid fraction, γ_{l}, in a control volume undergoing phase change can be evaluated using the following iterative expression [10]:

$$\gamma_{\mathrm{l}}^{n+1}=\gamma_{\mathrm{l}}^{n}+\frac{\theta^n-\theta_{\mathrm{PH}}}{1-\theta_{\mathrm{PH}}}\Omega^n(S_{\mathrm{w}})_{\mathrm{M}}\Pi, \tag{12}$$

with limitations expressed by equation (13),

$$0\leqslant\gamma_{\mathrm{l}}^{n+1}\leqslant\varepsilon. \tag{13}$$

The value of κ in the third term on the right hand side of equations (8) and (9) can be evaluated from the next equation.

$$\kappa=\varepsilon^3/(1-\varepsilon)^2\cdot(1-\gamma_{\mathrm{l}})^2/\gamma_{\mathrm{l}}^3. \tag{14}$$

In the expression (14), we adopt the Kozeny–Carman model [11] for the permeability because a maximum Reynolds number ($=d\cdot(u^2+v^2)^{1/2}/\nu$) is small, about 6.0, under conditions in the present study.

The initial conditions are set at

$$\tau=0,\quad U=V=0,\quad \theta=0,\quad \gamma_{\mathrm{l}}=0$$
$$\text{(in the entire region)} \tag{15}$$

and, the boundary conditions are listed in Table 1, where θ_{F} stands for the temperature of the fins and it can be evaluated from equation (11). The nondimensional temperature, θ, on the hot wall is set at unity except for a calculation, whose results are shown in Fig. 2, in which measured values are input as the hot wall temperature in the calculation and the calculated results are compared with experimental ones.

The velocity of a perfectly-solidified control volume with $\gamma_{\mathrm{l}}=0$ must vanish. This is automatically accomplished since the value of κ becomes infinity (see equation (14)) for $\gamma_{\mathrm{l}}=0$, and the Darcy term (resistance to the fluid flow) also becomes infinity, resulting in zero velocity in the control volume, as is seen from equations (8) and (9). The nondimensional governing equations were discretized based on the SIMPLER algorithm [12] with the power law for the convective terms, and they were solved iteratively. Detailed numerical procedures can be seen in refs. [12, 13]. The calculation was iterated at the same time-step until the following criteria were satisfied:

(i) for the velocities, U and V,

$$\frac{\max|\phi^{n+1}(I,J)-\phi^n(I,J)|}{\max|\phi^{n+1}(I,J)|}<10^{-4}, \tag{16}$$

(ii) for the temperature, θ, and the volumetric liquid fraction, γ_{l},

$$\frac{|\phi^{n+1}(I,J)-\phi^n(I,J)|}{|\phi^{n+1}(I,J)|}<10^{-4}, \tag{17}$$

(iii) and, for the dimensionless residual mass-source [12], b,

$$|b(I,J)|<10^{-3}, \tag{18}$$

where

$$b(I,J)=(U_{\mathrm{w}}-U_{\mathrm{e}})\Delta Y+(V_{\mathrm{s}}-V_{\mathrm{n}})\Delta X.$$

In the above expression, ΔX and ΔY stand for nondimensional lengths of a control volume in the x- and y-directions, respectively. The subscripts w, e, s and n mean west-, east-, south- and north-side control-volume faces, respectively.

Preliminary calculations were performed to determine the number of meshes. For ϕ of 0 and 180, 25 (x-direction) $\times 25$ (y-direction) and 30×40 nonuniform mesh-systems for the half region of the elemental region in Fig. 1(b), because of symmetry of the phenomena, were examined. Since the difference between the calculated results is very small, e.g. at $\tau=0.014$ the melting fraction, R, was 0.497 for the 30×40 mesh and 0.510 for the 25×25 mesh, the 25×25 mesh system was used for ϕ of 0 and 180 considering computational expense. For ϕ of 90, 30×20 and 40×30 mesh systems were used for pre-

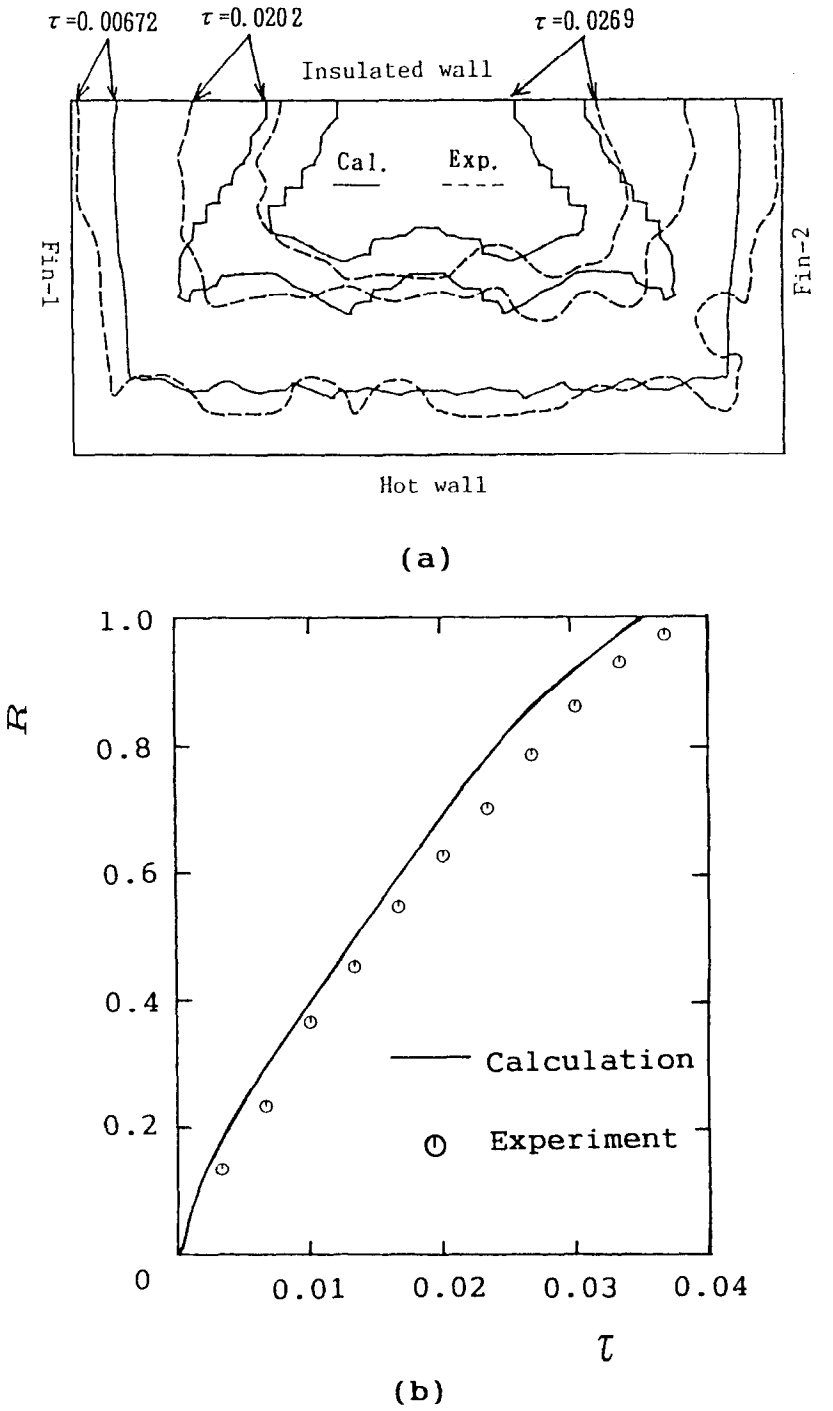

FIG. 2. Comparison between calculated and experimental results for the case with the conducting fins: (a) interface shapes and (b) melting fractions.

liminary calculations, and the 30×20 mesh system was chosen (at $\tau = 0.018$, the value of R was 0.505 for the 30×20 mesh system and 0.499 for the 40×30 mesh system). The increment of time, $\Delta\tau$, was changed from 1.0×10^{-7} to 2.0×10^{-5} during the calculations.

3. RESULTS AND DISCUSSION

3.1. *Comparison of numerical results and experimental ones*

To check the validity of the present numerical calculations, numerical results under several conditions were compared with experimental ones. An example is shown in Fig. 2. The conditions are as follows:

At $t = 0$ s: $T = T_i = -2$ °C, $t \geqslant 0$: $T_w = 20$ °C
$L_x = 0.1$ m, $L_z = 0.05$ m
material of the fins: brass
thickness of the fins: $\delta = 0.003$ m
particles: glass beads with diameter, d, of 0.012 m
fluid: pure water.

With these conditions the values of important nondimensional parameters become as follows:

$$R_{aM} = -9.07 \times 10^6, \quad P_r = 9.36, \quad D_a = 4.01 \times 10^{-5},$$

$$\varepsilon = 0.491, \quad \eta = 5.42, \quad \zeta_{sl} = 237.1, \quad (S_{te})_M = 0.251.$$

As expressed before, since $\beta_1 (= -0.678964520 \times 10^{-4})$ is used as the thermal expansion coefficient in the definition of Rayleigh number, R_{aM}, it has a negative value.

Now, Fig. 2(a) shows a comparison of timewise variations of interface shape, and Fig. 2(b) that of melting fractions.

The hot wall temperature in the experiment could not be set at the prescribed value, $T_w = 20$ °C, at $t = 0$ s, taking about two minutes to reach the value. So, in the calculation the measured value was used as the hot wall temperature. The calculated interface shapes, in general, agree well with the experimental ones obtained on photographs (see Fig. 2(a)), except in regions near the top insulated wall. The porosity, ε, near the regions is larger than that in other regions in the experiment so that there is more quantity of ice to be melted near the top wall, while in the calculation the porosity is assumed uniform and isotropic in the entire region for simplicity. The agreement of the melting fractions (Fig. 2(b)) is also good although there exists some difference due to the fact mentioned above. Figure 2 is an example for which the largest difference between calculated results and experimental ones was observed in the preliminary runs. In other example calculations with simpler conditions than that for the case of Fig. 2, i.e. the case of no porous particles (pure water only) and the case with small glass beads ($d = 2.9$ mm; for which natural convection was very weak), the agreement of the results was fairly good. Considering the many assumptions made in the calculations for simplicity, e.g. uniformity of the porosity and local thermal equilibrium, it can be said that the agreement is satisfactory even for the case shown in Fig. 2.

3.2. *Effect of the orientation of the hot wall*

Calculations were performed for three orientations of the hot wall, that is, melting from below, from the side and from above. The conditions are the same as those in Fig. 2, except that the initial temperature, T_i, is equal to the fusion temperature (0 °C), and that the wall temperature is assumed to be set at a prescribed value (step change), $T_w = 20$ °C, at $t = 0$ s. Figure 3 shows the case of melting from below ($\phi = 0°$). Since the phenomenon is symmetry about the vertical centerline, the velocity fields are shown in the left of the figure, and the isotherms in the right of it. At a very early stage (Fig. 3(a): $\tau = 0.0030$), since a melt layer above the hot wall is very thin, no natural convection is observed near the center of the hot wall. But, near the fin surface, a weak circulation is already observed near the base of the fin. This circulation induces a weak natural-convection cell on the hot wall near the fin base. The interface shape is still smooth with such weak cell. At $\tau = 0.0100$ (Fig. 3(b)) Bénard's-cell-type natural-convection cells appear above the hot wall, and the temperature distribution becomes irregular. The melting becomes faster in the regions where the hot liquid hits directly. And, it is also seen that the circulations along the fin surfaces become strong, and the melting near the fin tips is fast. At a late stage (Fig. 3(c): $\tau = 0.0243$), the many weak cells above the hot wall observed in Fig. 3(b) merge into very large cells, and they strongly interact with the large circulation near the fin surface. Therefore, the fluid flow becomes very complicated. The density-inversion region between $\theta = 0$ ($T = 0$ °C; at the solid/liquid interface) and $\theta = 0.2$ ($T = 4$ °C) is very small in the entire time so that it does not apparently affect the flow and temperature fields.

For comparison, temperature and flow fields for the case with the nonconducting fins at $\tau = 0.01$, corresponding to Fig. 3(b), are shown in Fig. 4. At this period, the thickness of the melt above the hot wall is almost the same as that in Fig. 3(b), except near the fins. At very early stages (not shown here) the melting above the hot wall was slightly faster for the case with the conducting fins than that for the case with the nonconducting fins. This is because the convection above the hot wall for the case with the conducting fins is accelerated by the circulation along the fin surface. Comparison of Fig. 4 with Fig. 3(b) indicates that the conducting fins act well to melt ice along the fin surfaces for the melting from below.

Figure 5 shows the case of melting from the side ($\phi = 90°$). At $\tau = 0.0030$ (Fig. 5(a)), a weak circulation along the hot wall is observed, and the hot fluid near the top of the hot wall protrudes slightly toward the insulated wall. But, the circulation is still very weak at this early stage so that the irregularity

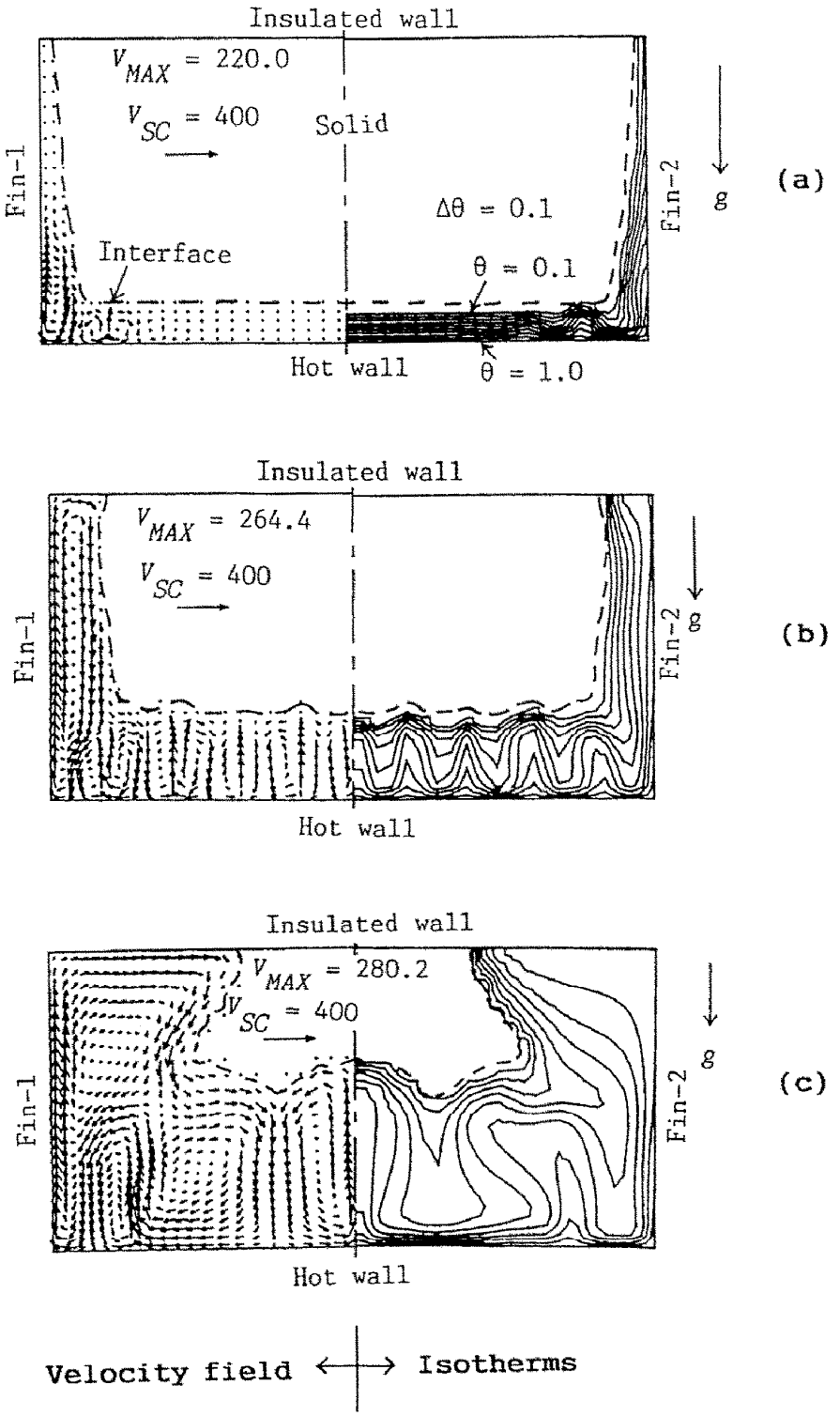

FIG. 3. Timewise variations of velocity and temperature fields in the case with the conducting fins for $\phi = 0°$; (a) $\tau = 0.0030$, (b) $\tau = 0.0100$ and (c) $\tau = 0.0243$.

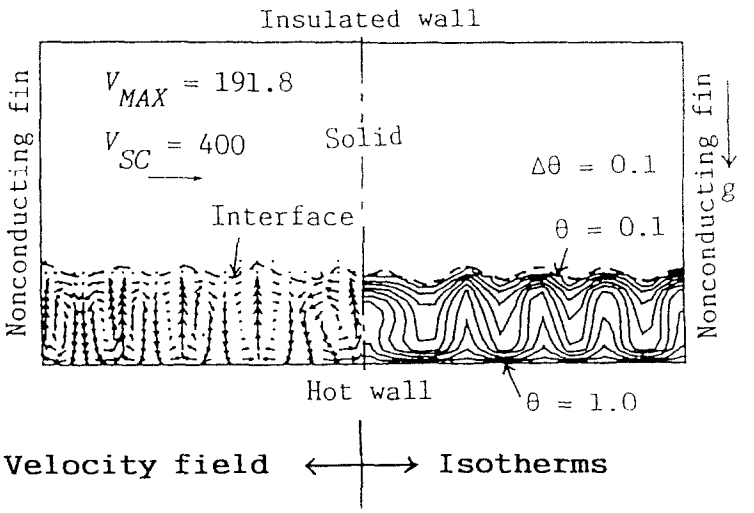

FIG. 4. Velocity and temperature fields at $\tau = 0.0100$ in the case with the nonconducting fins for $\phi = 0^\circ$, corresponding to Fig. 3(b).

of the interface shape is small. As time proceeds, the circulation becomes stronger, and the melting near the top fin develops very quickly, as shown in Fig. 5(b) at $\tau = 0.0180$. And, at this stage, convection cells due to thermal instability are observed above the bottom fin, and the cells enhance the melting there. In Fig. 5(c) at a late stage ($\tau = 0.0336$), the thickness of the melt above the bottom fin is considerable.

Figure 6 shows the case with the nonconducting fins at $\tau = 0.0180$, corresponding to Fig. 5(b). Comparing the two figures, it is seen that the melting near the top fin is faster for the case with the conducting fins (Fig. 5(b)) than the case with the nonconducting fin (Fig. 6). But, the difference became smaller with time due to thermal stratification near the top fin. Hence, the bottom conducting fin begins to play an important role for the heat transfer enhancement as time proceeds as shown in Fig. 5(c).

For the case of the melting from above (Figs. 7(a)–(c): $\phi = 180^\circ$), only very weak natural convection is observed even for late stages since the melt layer is thermally almost stable, and heat conduction is predominant. Therefore, the interface shape is very similar to that for the solidification process [7]. The density-inversion region is larger than those for other orientations of the hot wall (compare the region between the solid/liquid interface and the isotherm of $\theta = 0.2$ in Fig. 7(c) with those in Figs. 3(c) and 5(c)), but it still occupies only a small portion of the entire melted region, and therefore it does not give a noticeable effect on the flow and temperature fields.

From Fig. 8 for the case with the nonconducting fins corresponding to Fig. 7(b), it is seen that the thickness of the melt layer below the hot surface is almost the same as that in Fig. 7(b) except near the fin surfaces. Since the melting is very slow for $\phi = 180^\circ$ in the case of the nonconducting fins, the effect of the attached conducting-fins on the heat-transfer enhancement largely appears.

3.3. *Timewise variations of mean Nusselt number and melting fraction*

Figures 9(a)–(c) show timewise variations of a mean Nusselt number over the hot wall for the case with the conducting fins, $(Nu)_w$ (solid lines), the sum of mean Nusselt numbers over the two fin surfaces, $(Nu)_F$ (dashed-two-dotted lines), as well as a mean Nusselt number over the hot wall for the case with the nonconducting fins, $(Nu)_w$ (dashed lines), for comparison. The definition of $(Nu)_w$ is

$$(Nu)_w = \int_0^1 (Nu)_w \, dX,$$

where

$$(Nu)_w = \frac{h_w L_c}{\lambda_l} = -\frac{L_c}{L_y}\left(\frac{\partial \theta}{\partial Y}\right)_{Y=0}.$$

Taking fin-1 (see Fig. 1) as an example, the mean Nusselt number over the fin surface is defined as follows (heat flux flowing into the considered element is assumed positive):

$$(Nu)_{F1} = \frac{L_y}{L_x}\int_0^{L_y/L_c} (Nu)_{F1} \, dY,$$

where

$$(Nu)_{F1} = \frac{h_{F1} L_c}{\lambda_l} = -\frac{L_c}{L_x}\left(\frac{\partial \theta}{\partial X}\right)_{X=0}.$$

Now, for the melting from below, $\phi = 0^\circ$ (Fig. 9(a)), $(Nu)_w$ for the case with the conducting fins (the solid line) abruptly decreases with increasing time

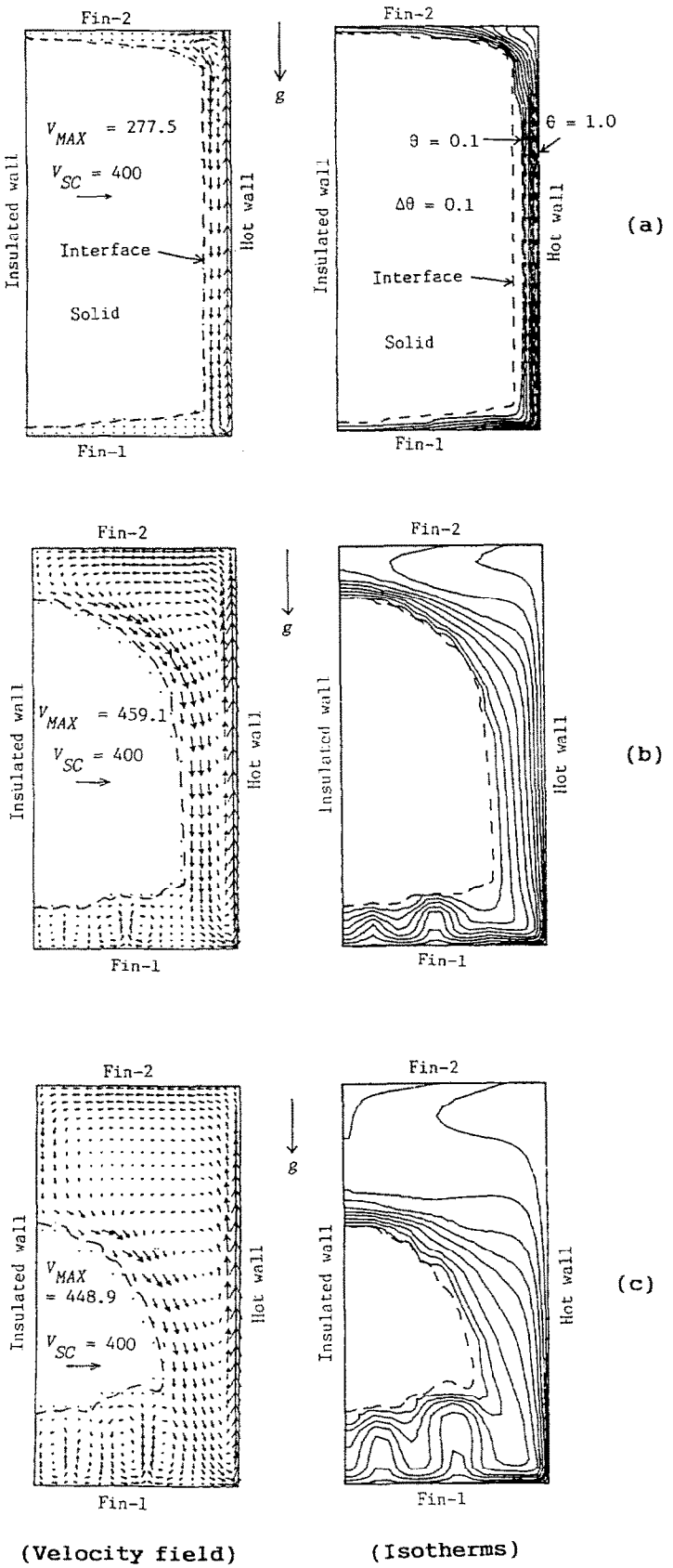

FIG. 5. Timewise variations of velocity and temperature fields in the case with the conducting fins for $\phi = 90°$: (a) $\tau = 0.0030$, (b) $\tau = 0.0180$ and (c) $\tau = 0.0336$.

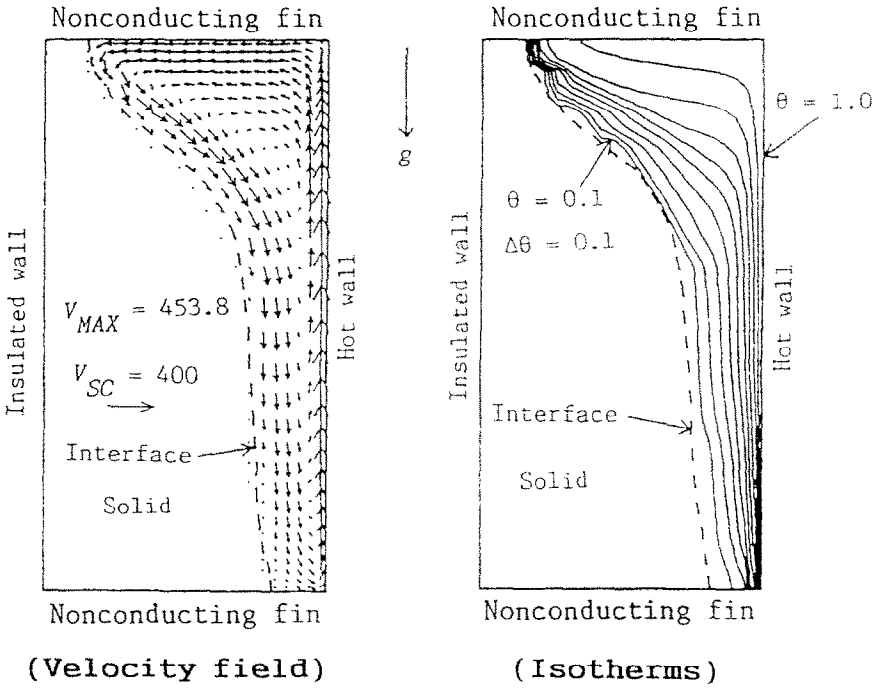

FIG. 6. Velocity and temperature fields at $\tau = 0.0180$ in the case with the nonconducting fins for $\phi = 90°$, corresponding to Fig. 5(b).

during the early stages, and then increases. This increase is due to the generation of many convection cells above the hot wall as shown in Fig. 3(b). The increase in $(Nu)_w$ occurs earlier and the increasing rate is smaller in comparison with the case for the nonconducting fins (the dashed line). This is because for the case with the conducting fins the cells above the hot wall are induced by the circulations along the fins during very early stages, and become stronger after the thickness of the melt layer on the hot wall becomes larger and the Rayleigh number based on the thickness exceeds a critical value. On the other hand, in the case with the nonconducting fins, the onset of the convection cells above the hot wall is purely due to the thermal instability in the melt.

After the maximum value is reached, the value of $(Nu)_w$ for the case with the conducting fins slightly decreases, and then is kept almost constant for $\tau > 0.01$ because the convection becomes stronger as the melting progresses, in spite of the fact that the distance between the interface and the hot wall becomes larger. The fluctuation of $(Nu)_w$ for $\tau > 0.01$ is due to the changes in the flow structure and the number of cells above the hot wall with time. For the case with the nonconducting fins the trend of the timewise variation of $(\bar{N}u)_w$ is similar with some delay of time to that for the case with the conducting fins.

The value of $(\bar{N}u)_F$ decreases during early periods, and then remains almost constant for $\tau > 0.01$, revealing the effectiveness of the fins. The abrupt decrease in $(Nu)_F$ near $\tau = 0.01$ is due to the fact that the strong circulations along the fins make the melting very fast, resulting in a sudden increase in the distance between the interface and the fin surfaces, especially near the fin tips.

For the melting from the side, $\phi = 90°$ (Fig. 9(b)), the value of $(Nu)_w$ for the case with the conducting fins is kept almost constant for $\tau > 0.005$, although the value is smaller than that in Fig. 9(a), due to the strong circulation along the hot surface and the effect of the strong convection-cells near the bottom fin, as shown in Fig. 5(c). It is also seen that the value of $(Nu)_w$ for the case with the nonconducting fins is larger than that for the conducting fins, and the value of $(Nu)_F$ is almost the same as that of $(\bar{N}u)_w$ for late stages, meaning large heat transfer augmentation by the attached fins.

In the case of the melting from above, $\phi = 180°$ (Fig. 9(c)), the values of $(Nu)_w$ for both types of the fin decreases monotonously with increasing time, and they become very small at late stages, while the value of $(Nu)_F$ is maintained larger than the values of $(Nu)_w$. Hence, for this orientation of the hot wall, the effect of the fins on the heat transfer augmentation is fairly large.

Finally, the timewise variations of the melting fractions for the three orientations of the hot wall are shown in Figs. 10(a)–(c), where R is defined as the melted volume divided by the total volume of the element. The solid lines represent the case with the

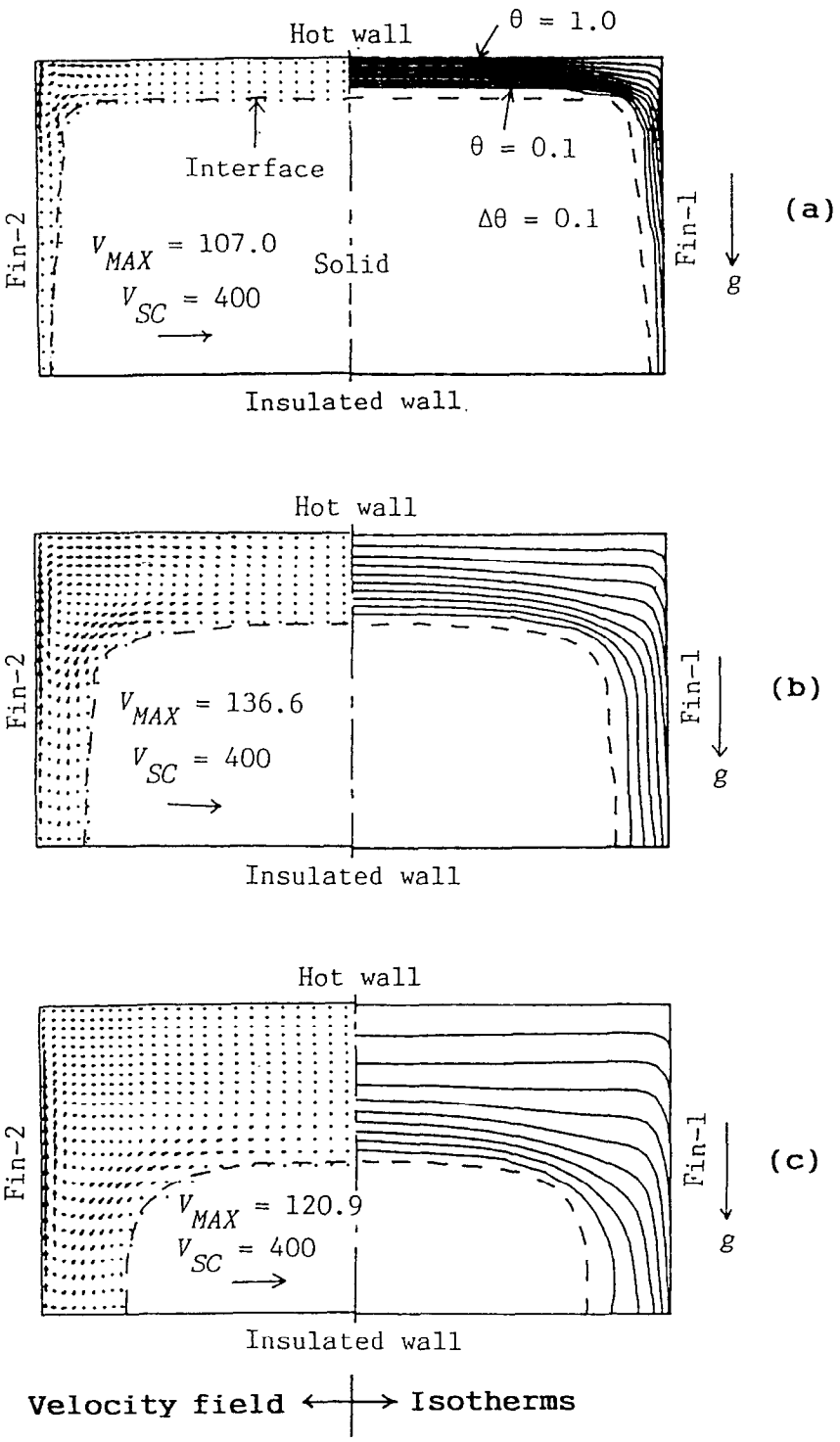

FIG. 7. Timewise variations of velocity and temperature fields in the case with the conducting fins for $\phi = 180°$: (a) $\tau = 0.0030$, (b) $\tau = 0.0160$ and (c) $\tau = 0.0403$.

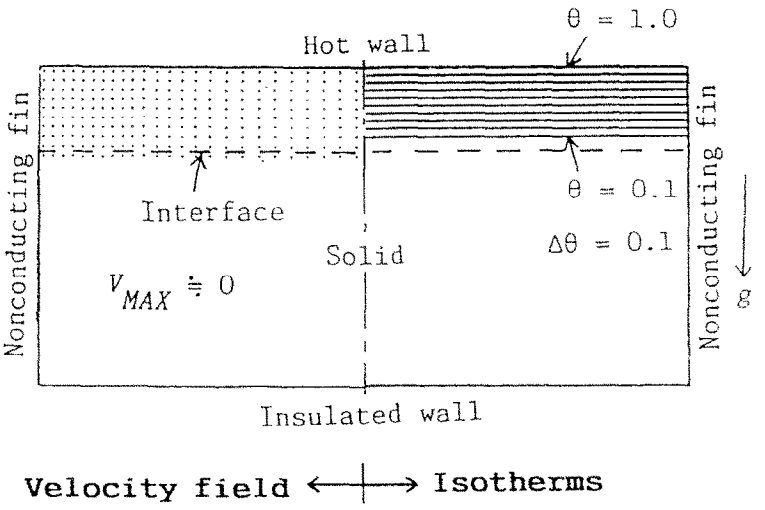

FIG. 8. Velocity and temperature fields at $\tau = 0.0160$ in the case with the nonconducting fins for $\phi = 180°$, corresponding to Fig. 7(b).

conducting fins, and the broken lines the case with the nonconducting fins. From the figures it is seen that during $\tau < 0.005$ the values of R for the cases with the conducting fins (the solid lines) are almost the same, regardless of the orientation of the hot wall, and the values are slightly larger than those for the case with the nonconducting fins. As time proceeds, the value of R increases linearly for the melting from below (Fig. 10(a)) because the convection cells above the hot wall and the circulations along the fins impinge a large surface area on the solid/liquid interface as shown in Fig. 3. For the melting from the side (Fig. 10(b)) the increasing rate of R is slightly smaller than that in Fig. 10(a). For the melting from above (Fig. 10(c)) it becomes quite small at late stages, and the shapes of the curves are very similar to those for solidification processes. Comparing the values of R for the cases with the conducting and nonconducting fins, it is seen that the difference is the smallest for the melting from below since natural convection above the hot wall is very strong, and it is the largest for the melting from above because heat conduction is predominant. Thus, the effectiveness of the attached conducting fins appears very clearly for the case of melting from above.

4. CONCLUSIONS

Calculations were performed for the melting of ice in a porous medium surrounded by a finned surface and an opposing insulated surface. The effect of the orientation of the hot surface on the flow and temperature fields, on averaged Nusselt numbers over the hot and fin surfaces, and on a melting fraction was examined. Furthermore, comparing the case with nonconducting fins, it was shown that the effectiveness of the conducting fins is changed with the orientation of the hot surface. Based on the results obtained the conclusions are summarized as follows:

(1) For the melting from below, strong circulations along the fins are generated, and the melting near the fins is enhanced, especially near the tip of the fins. Since these circulations induce convection cells above the hot surface, the onset of the cells is earlier than that for the case with the nonconducting fins.

(2) When the melting is initiated from the side, ice near the upper conducting fin melts faster than that for the case with the nonconducting fins during early times, but the difference becomes smaller with increasing time due to thermal stratification. Very strong convection-cells generated above the lower conducting fin due to thermal instability play an important role in melting ice. Thus, in this orientation of the hot surface the lower conducting fin has a large effect on an increase in the melting rate.

(3) For the melting from above, although weak natural convection arises near the conducting fins, the heat transfer is, in general, dominated by conduction. Hence, the melting below the hot surface is very slow, and the effectiveness of the attached conducting fins appears clearly, compared with the melting processes with the other orientations of the hot surface.

(4) From the timewise variations of the mean Nusselt numbers over the hot surface, $(\overline{Nu})_w$, and over the conducting fins, $(\overline{Nu})_f$, the value of $(\overline{Nu})_w$ for the case with the conducting fins is larger than the value of $(\overline{Nu})_f$ for a long period for the melting from below. For the melting from the side, these values are almost the same, and for the melting from above $(\overline{Nu})_f$ is much larger than $(\overline{Nu})_w$. The difference between the melting fractions for the cases with the conducting

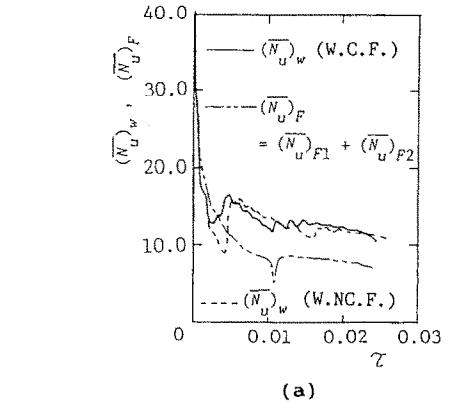

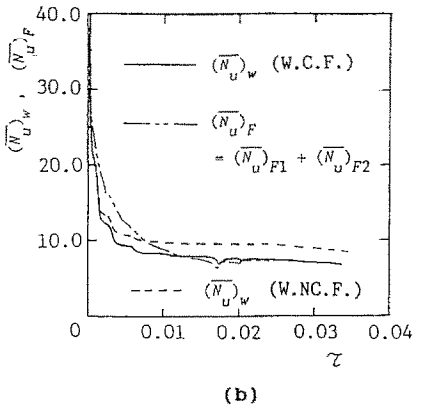

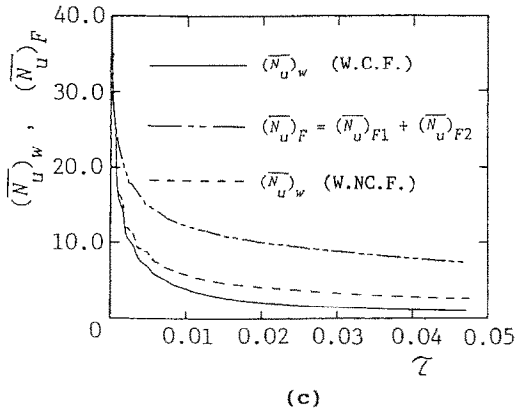

FIG. 9. Comparison of mean Nusselt numbers: (a) $\phi = 0°$, (b) $\phi = 90°$ and (c) $\phi = 180°$. W.C.F.: With conducting fins; W.NC.F.: With nonconducting fins.

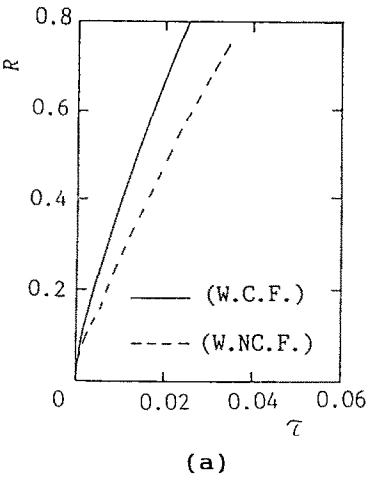

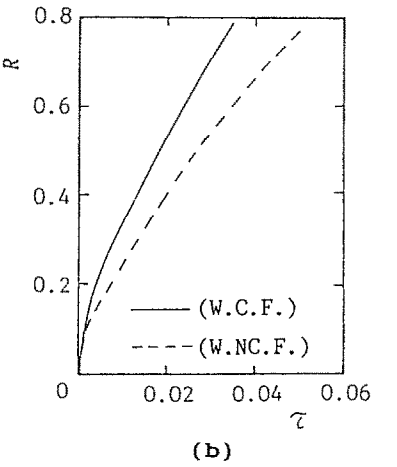

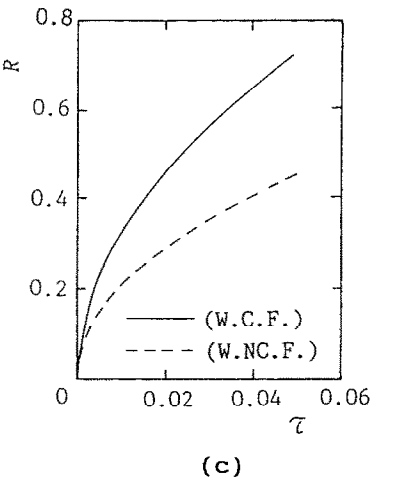

FIG. 10. Comparison of melting fractions: (a) $\phi = 0°$, (b) $\phi = 90°$ and (c) $\phi = 180°$. W.C.F.: With conducting fins; W.NC.F.: With nonconducting fins.

and nonconducting fins becomes larger for the melting from above than those for other orientations of the hot surface. Therefore, the effect of the attached conducting fins is considerable for the melting from above.

REFERENCES

1. S. Chellaiah and R. Viskanta, Freezing of saturated and superheated liquid in porous media, *Int. J. Heat Mass Transfer* **31,** 321–330 (1988).
2. C. Beckermann and R. Viskanta, Natural convection solid/liquid phase change in porous media, *Int. J. Heat Mass Transfer* **31,** 35–46 (1988).
3. A. Sasaki, S. Aiba and S. Fukusako, Freezing heat transfer in water-saturated porous media in a vertical rectangular vessel, *Wärme- und Stoffübertragung* **27,** 289–298 (1992).
4. M. Okada and T. Fukumoto, Melting around a horizontal pipe embedded in a frozen porous medium, *Trans. Japan Soc. Mech. Engrs* **48B,** 2041–2049 (1982) (in Japanese).
5. M. Sugawara, H. Inaba and N. Seki, Effect of maximum density of water on freezing of a water-saturated horizontal porous layer, *J. Heat Transfer* **110,** 155–159 (1988).
6. X. Xhang and T. H. Nguyen, Melting of ice in a porous medium heated from below, *Int. J. Heat Mass Transfer* **34,** 389–405 (1991).
7. K. Sasaguchi, K. Kusano and N. Nishimizu, Solid–liquid phase change heat transfer in porous media (Effects of fins on the solidification process), *Trans. Japan Soc. Mech. Engrs* **59B,** 1712–1718 (1993) (in Japanese).
8. W. D. Bennon and F. P. Incropera, A continuum model for momentum, heat and species transport in binary solid–liquid phase change systems—I. Model formulation, *Int. J. Heat Mass Transfer* **30,** 2161–2170 (1987).
9. T. Fujii, *Advances in Heat Transfer*, Vol. 3, p. 66, Yokendo, Tokyo, Japan (1974) (in Japanese).
10. V. R. Voller, Fast implicit finite-difference method for the analysis of phase change problems, *Numer. Heat Transfer* **17B,** 155–169 (1990).
11. S. Egrun, Fluid flow through packed columns, *Chem. Engng Progress* **48,** 89–94 (1952).
12. S. V. Patankar, *Numerical Heat Transfer and Fluid Flow*, Hemisphere, New York (1980).
13. H. Takeo, Numerical analysis on solid/liquid phase change heat transfer in porous media, Master Eng. Thesis, Kumamoto University, Kumamoto, Japan (1991) (in Japanese).